

# Photoacoustic mammography laboratory prototype: imaging of breast tissue phantoms

Srirang Manohar  
Alexei Kharine  
Johan C. G. van Hespén  
Wiendelt Steenbergen  
Ton G. van Leeuwen

University of Twente  
Biophysical Engineering Group  
Faculty of Science and Technology  
P.B. 217  
7500AE Enschede, The Netherlands  
E-mail: s.manohar@tnw.utwente.nl

**Abstract.** We present a laboratory version of a photoacoustic mammoscope, based on a parallel plate geometry. The instrument is built around a flat high-density ultrasound detector matrix. The light source is a Q-switched Nd:YAG laser with a pulse duration of 5 ns. To test the instrument, a novel photoacoustic phantom is developed using poly(vinyl alcohol) gel, prepared by a simple procedure that imparts optical scattering suggestive of breast tissue to it without the requirement for extraneous scattering particles. Tumor simulating poly(vinyl alcohol) gel spheres appropriately dyed at the time of preparation are characterized for optical absorption coefficients. These are then embedded in the phantom to serve as tumors with absorption contrasts ranging from 2 to 7, with respect to the background. Photoacoustic studies in transmission mode are performed, by acquiring the laser-induced ultrasound signals from regions of interest in the phantom. Image reconstruction is based on a delay-and-sum beamforming algorithm. The results of these studies provide an insight into the capabilities of the prototype. Various recommendations that will guide the evolving of our laboratory prototype into a clinical version are also discussed. © 2004 Society of Photo-Optical Instrumentation Engineers. [DOI: 10.1117/1.1803548]

**Keywords:** photoacoustic; laser-induced ultrasound; ultrasound detector; detector matrix; poly(vinyl alcohol) gel; breast phantom.

Paper 04036 received Mar. 15, 2004; revised manuscript received Jun. 15, 2004; accepted for publication Jun. 28, 2004.

## 1 Introduction

Room for improvement in the current practice of breast cancer screening and diagnosis, and the fact that breast cancer is an enormous burden on society, have been the stimuli for relentless efforts on two fronts. On the one, the current state of the art in detection and diagnosis, using x-rays, ultrasound, and magnetic resonance, is being pushed forward. On the second front, there is a quest for new modalities that can address the limitations and drawbacks of the current technologies.

Of the myriad alternative techniques,<sup>1</sup> a promising area is optical imaging, which uses near-infrared (NIR) light as the probe. Optical imaging is a simple, low-cost and risk-free technique that does not use ionizing radiation. The technique involves the detection of photons that propagate through the breast, and using models based on the nature of their propagation, reconstructing the optical properties of the illuminated tissue. It has been demonstrated in several studies<sup>2–4</sup> that tumors possess absorption and scattering contrast compared to healthy, background tissue for NIR light due to fundamental changes associated with tumor growth. These changes may be abnormal structural features, enhanced vascularization, and differences in blood oxygen consumption at tumor sites. In addition to intrinsic contrast of tumors, there have been efforts to improve the sensitivity of the technique with the use of

contrast enhancers such as indocyanine green (ICG), intravenously administered to subjects.<sup>5,6</sup>

However, light propagation in biological tissue is highly scattering, which results in poor resolution. There have been several approaches to surmount the resolution impediment—computational resolution enhancement<sup>7,8</sup> using continuous waves (cw), and additional technological and methodological modifications to the cw case to permit time-domain<sup>9,10</sup> and frequency-domain measurements<sup>11,12</sup>.

Improving spatial resolution and discriminating between absorption and scattering remain the biggest challenges that are faced by optical imaging. A technique that can avail the endogenous contrast exhibited by tumors to NIR light, without having to combat the problems associated with scattering, is photoacoustic imaging. In this technique, the interaction of photons with an object of interest is studied not by detecting and analyzing photons that have escaped the interaction, as in conventional optical techniques. On the contrary, the data are obtained as a direct measure of those photons absorbed by the structure. The absorbed photon energy is thermalized, resulting in a local deposition of heat. Under conditions of adiabatic heating and stress confinement, the resulting localized temperature rise causes stress transients to be set up by thermal expansion. This propagates through the embedding medium as ultrasound to be detected at the surface. Thus, in this hybrid technique, optical absorption contrast of tumors on the one hand, and lower acoustic scattering in tissue on the other

Address all correspondence to Srirang Manohar, Univ. of Twente, Biofysische Techniek, Technische Natuurwetenschappen, P.O. Box 217, NL-7500 AE Enschede, Netherlands. Tel: +31-53-489-3164; Fax: +31-53-489-1105; E-mail: S.Manohar@tn.utwente.nl

hand, are brought together. Since the technique does not “look” for photons and the resulting ultrasound propagates with low scattering through tissue, photoacoustics yields higher resolution than purely optical techniques.

The hypothesis of using photoacoustics for breast tumor detection, based on increased optical absorption by hemoglobin in the enhanced cancer vascularization, has been demonstrated in restricted studies by the group of Oraevsky and his collaborators.<sup>13,14</sup> They used an arc-shaped 32-element piezoelectric polyvinylidene fluoride (PVDF) transducer array in their clinical prototype, the laser optoacoustic imaging system (LOIS). The group has experimented with two modes, transmission and reflection, and used wavelengths of 1064 and 760 nm for the light excitation.

There is also expected to be an increased ionic water content associated with the neovascularization. This has been demonstrated by the group of Kruger<sup>15–17</sup> using radio waves (434 MHz) for ultrasound generation in a few studies using a thermoacoustic computed tomography (TCT) scanner. This device uses an arrangement of three planar arrays comprising 128 elements in total, which when rotated around the pendant breast, provide a uniform detection coverage over a hemispherical surface. (In this work, the term photoacoustic is used equivalent to optoacoustic and thermoacoustic. The rationale behind this is the fact that the term photoacoustic conveys the quintessential feature of the technique: the incident energy is in the form of photons of the electromagnetic spectrum, whether in the optical, microwave, or radiowave range, and the data are obtained as acoustic signals.)

However, there have been as yet no large published clinical trials from either group, and the technique is in its incipient stages; the original patents being issued as late as 1998.<sup>18,19</sup>

In this work, we introduce a laboratory version of a photoacoustic (PA) mammoscope based on a parallel plate geometry, built around a flat high-density ultrasound detector matrix. The instrument uses NIR excitation at 1064 nm. We also describe a photoacoustic breast tissue phantom developed to validate the feasibility of the instrument in detecting deeply embedded inhomogeneities. We present photoacoustic studies on this phantom, which provide an insight into the capabilities of the instrument. Various recommendations that will guide the evolving of our laboratory prototype into a clinical version are also discussed.

## 2 Methods and Materials

### 2.1 Photoacoustic Imaging

The field of radiation-induced ultrasound for biomedical studies was pioneered by Bowen et al.<sup>20,21</sup> in 1981, using microwaves. In 1994, Kruger<sup>22</sup> and Oraevsky et al.<sup>23</sup> explored the phenomenon using optical radiation. Since then, photoacoustics has been applied in a variety of biomedical themes. Applications have been seen in small-animal imaging;<sup>24,25</sup> imaging of human blood vessels;<sup>26</sup> temperature<sup>27</sup> and photo-coagulation<sup>28</sup> monitoring during ophthalmic laser therapy; burn depth estimation;<sup>29</sup> port-wine stain depth estimation;<sup>30</sup> glucose monitoring;<sup>31,32</sup> blood oxygenation monitoring;<sup>33,34</sup> and mammography.<sup>13,17</sup>

The photoacoustic phenomenon is the result of photothermal heating. Photothermal heating follows from absorption of

optical energy and subsequent nonradiative deexcitation of the excited internal energy levels. The resulting temperature rise produces thermal expansion, which under certain conditions, produces a pressure transient that propagates as ultrasound. The shape, amplitude, and duration of the ultrasound pulse are governed by the geometry and dimensions of the absorber, its optical and acoustic properties, and properties of the exciting beam such as pulse characteristics and local fluence rate.

Consider a situation when an absorbing sphere in a less absorbing embedding medium is illuminated with pulsed laser light. Let the laser pulse duration  $\tau_p$  satisfies the following inequality,

$$\tau_p \ll \tau_a \ll \tau_h, \quad (1)$$

where  $\tau_h$  is the thermal diffusion time and  $\tau_a$  is the acoustic transit time. The symbols and terms used here and later on are explained in Table 1. Equation (1) describes the regime of thermal and stress confinement, which is characterized by insignificant heat diffusion and pressure relaxation during the time scale of the laser (heating) pulse duration. In such a case, the mechanisms leading to pressure generation are efficient to yield higher amplitudes of the ultrasound than when the heat and pressure are allowed to “leak” during the heating pulse. Photoacoustic theory, when applied to the spherical absorber under the irradiation conditions described by Eq. (1), yields the following expression for the pressure,<sup>35,36</sup>

$$p(r, t) = -P_{\max} \frac{\sqrt{2ev}}{r_o} \exp\left\{-\left[\frac{v}{r_o}\left(t - \frac{r}{v}\right)\right]^2\right\}; \quad (2)$$

$$P_{\max} = -P_{\min} = \frac{\beta E_a v^2}{(2\pi)^{3/2} \sqrt{e c_p} r_o^2 r}. \quad (3)$$

This expression describes a positive (compression) peak followed by a negative (rarefaction) peak.<sup>35,36</sup> The peak amplitudes are located at,

$$t = \frac{r}{v} \pm \frac{\tau_{pp}}{2}, \quad \text{where } \tau_{pp} = \sqrt{2} \frac{r_o}{v} \quad \text{or } \sqrt{2} \tau_a. \quad (4)$$

Thus, the ultrasound pulse has a bipolar shape with a duration that can be related to the dimensions of the absorbing sphere, and with an amplitude that depends on its absorption coefficient.

The ultrasound that is produced is then detected at the surface of the embedding medium using either piezoelectric<sup>37,38</sup> or optical detection<sup>39–42</sup> schemes.

#### 2.1.1 Image reconstruction

Reconstruction of absorbers is performed using the delay-and-sum beamforming algorithm.<sup>43</sup> This applies a phase-array approach to focus the sensitivity of the detectors in a planar matrix to single volume elements or voxels in turn, into which the investigated bulk volume is assumed to be divided. This is performed off-line for the acquired signals from a set of detectors. Each voxel is thus probed as a potential source of photoacoustic signals, which for spherical sources are bipolar.

The output of the beamformer  $S^V(t)$ , can be expressed as,

**Table 1** Nomenclature and symbols.

$\tau_p$	laser pulse width (s)	$r$	distance to field point (m)
$\tau_a = r_o / v$	acoustic transit time through a sphere (s)	$t$	time (s)
$\tau_h = r_o^2 / \kappa_t$	thermal diffusion time (s)	$\beta$	thermal expansion coefficient ( $\text{cm}^{-3}$ )
$r_o$	radius of sphere (m)	$E_a$	absorbed laser energy (J)
$v$	acoustic velocity ( $\text{m s}^{-1}$ )	$\tau_{pp}$	peak-peak time (s)
$\kappa_t = K / \rho c_p$	thermal diffusivity ( $\text{m}^2 \text{s}^{-1}$ )	$S^V$	beamformer output
$K$	thermal conductivity ( $\text{J m}^{-1} \text{s}^{-1}$ )	$w_i^V$	weight factor
$\rho$	mass density ( $\text{kg m}^{-3}$ )	$S_i$	signal (V)
$c_p$	specific heat capacity ( $\text{J kg}^{-1} \text{K}^{-1}$ )	$\delta_i^V$	time delay (s)
$p$	PA pressure disturbance (Pa)	$i$	specific detector element
$P_{\max}$	maximum amplitude of PA pressure (Pa)	$V$	specific voxel
$P_{\min}$	minimum amplitude of PA pressure (Pa)	$\mu_a$	absorption coefficient ( $\text{mm}^{-1}$ )
$e$	$\exp(1)$	$\mu'_s$	reduced scattering coefficient ( $\text{mm}^{-1}$ )

$$S^V(t) = \frac{\sum_i w_i^V S_i(t + \delta_i^V)}{\sum_i w_i^V}, \quad (5)$$

where  $w_i^V$  is a weight factor,  $S_i(t)$  is the signal, and  $\delta_i^V$  is the delay applied, with  $i$  being a specific detector element and  $V$  a specific voxel. As seen in Eq. (5), signal traces are delayed appropriately to account for the acoustic transit time from a certain voxel to each of the detectors. The individual signals are also treated by applying weights to account for the angular/directional sensitivity of the elements. The weight factors depend on the distance between the voxel plane and the detector plane, and the angle between the voxel and each detector element. These weights are available either from prior experiment or from simulation.<sup>43</sup> The signals are then windowed in time corresponding to the dimensions of the voxel. The delayed, weighted, and windowed signals from all the detectors are then summed. The peak-peak value of the resultants are normalized with the weights to make them independent of the actual set of detectors. The net result is that a source, if present in the voxel, will become conspicuous by a constructive interference from PA signals recorded by more than one detector, while noise will be suppressed. This procedure is applied to every voxel in turn to obtain a 3-D reconstruction of the investigated volume.

## 2.2 Instrumentation

### 2.2.1 Envisaged photoacoustic mammoscope

A schematic of the proposed mammoscope based on a parallel plate geometry is shown in Fig. 1(a).

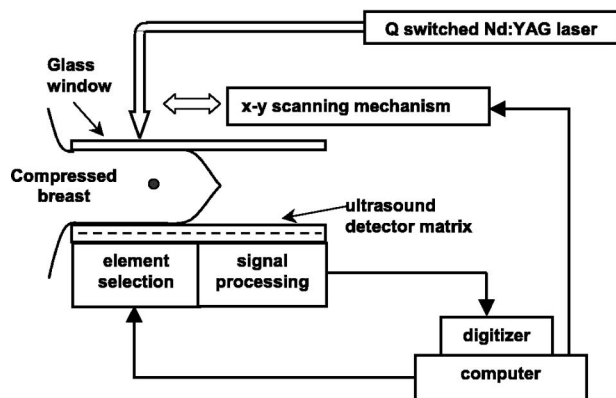
The breast is held between a transparent glass plate and an ultrasound detector matrix. A scanning system translates a pulsed laser beam in two dimensions to illuminate the top surface of the breast through the glass window. The breast is compressed gently to obtain good acoustic contact with the

detector matrix. The signals from the ultrasound detector are acquired and analyzed using a personal computer.

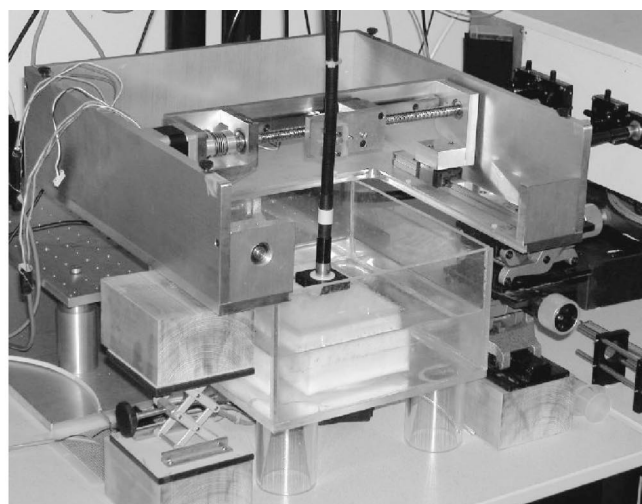
### 2.2.2 Laboratory prototype

The laboratory implementation is shown in Fig. 1(b). The light source is a Q-switched Nd:YAG laser (Quantel Brilliant-B, Paris) operating at 1064 nm with a pulse duration of 5 ns and a repetition rate of 10 Hz. The pulse width ( $\tau_p$ ) of the laser fulfills the conditions for thermal and stress confinement as per Eq. (1). The choice of laser wavelength is dictated by the fact that mammography involves imaging through large volumes of tissue; light penetrance in breast tissue is expected to be maximum in the 1000 to 1100 nm region.<sup>2</sup> The light beam is coupled to a liquid light guide (LLG). The LLG (Oriental Instruments, Stratford) of diameter 8 mm is mounted on a holder, which forms a payload to a stepper motor-driven scanning system. The scanning system is based on lead screws providing a stroke of 200×200 mm, which thus permits the LLG to be scanned across the surface of a breast simulating phantom. There is no glass plate and no requirement for any compression in the prototype, since the subjects are liquid or solid phantoms that are placed in an imaging tank. The tank is constructed from Perspex, with an aperture at the bottom, through which the detector matrix is fitted.

The heart of the instrument is a PVDF-based hydrophone matrix developed by the Lunar Division of General Electric (Madison, Wisconsin). The matrix is an ultrasound receiver in the Achilles InSight™, for bone-density measurements for the purpose of osteoporosis detection. (Further information regarding the bone ultrasonometer, the Achilles InSight™, can be found at the Internet site: [www.gemedicalsystems.com/rad/bonedens/peripheral/insight.html](http://www.gemedicalsystems.com/rad/bonedens/peripheral/insight.html).) It consists of 590 elements comprising spring-loaded contacts on the uncoated face of a single-side metallized PVDF film of thickness 110 μm. The film is supported on its free surface by an 18.6-mm-thick



(a)



(b)

**Fig. 1** (a) Schematic diagram of the envisaged photoacoustic mammoscope, based on a parallel plate geometry. (b) A photograph of the laboratory implementation. The experiments are conducted in a transmission mode by positioning the liquid light guide at different points above the phantom. The phantom is contained with water in a Perspex tank, at whose bottom the detector matrix is fixed. The face of the matrix is flush with the floor of the tank, and makes good contact with the bottom surface of the phantom.

layer of a proprietary material that forms the face of the unit. This layer serves as a protective layer, and possesses acoustic properties close to those of tissue. The detector elements are  $2 \times 2$  mm square and arranged in a Cartesian grid with an interelement separation of 3.175 mm. The active area of the detector matrix is approximately 90 mm in diameter.

In the photoacoustic prototype, the receiver unit is sealed through an aperture at the bottom of the imaging tank, so that the free surface of the protective layer is flush with the floor of the tank. The tank may be filled with a liquid phantom such as Intralipid™, but can also accommodate a solid phantom (discussed later) for experiments.

The frequency response of an individual element is centered around 500 KHz with a  $-3$ -dB bandwidth of 80%. The signal processing and multiplexing schemes are on board and provide the capability of accessing one element at a time. The required element can be activated with a set of logic levels on the appropriate control pins of the device. The control lines of the device are controlled via a digital input-output card (NI-6305, National Instruments, Austin, Texas) in the PC. The data line is fed to one channel of a dual-channel 100-MHz, 100-MS/s, 8-bit digitizer (NI-5112, National Instruments) card in the PC. The PC runs a LABView™ (National Instruments) program that controls the scanning system, the detector array, and digitizer.

### 2.3 Breast Phantom with Embedded Absorbing Inhomogeneities

To validate the feasibility of the laboratory prototype in detecting deeply embedded tumors, we first performed phantom studies. A phantom suitable for photoacoustic studies must possess not only the optical properties of tissue but also the acoustic properties. The breast tissue phantom we developed was based on poly(vinyl alcohol) (PVA) gel, recently shown

by us as being able to be prepared with properties of tissue<sup>44</sup> relevant to photoacoustics, and possessing superior mechanical properties to conventional gel phantoms.

#### 2.3.1 Turbid gels to mimic breast tissue—method 1

Poly(vinyl alcohol) gel formation, achieved by cross-linking of the polymer chains in an aqueous solution, is most easily accomplished by a process of repeatedly freezing and thawing the solution.<sup>45</sup> In addition to the formation of the cross-links, crystallites are also formed that serve to further increase the dimensionality and reinforce the gel structure. The number, size, and stability of the crystallites increase with increasing number of freeze-thaw cycles resulting in rigidification of the gel.<sup>46</sup> An attendant phenomenon to this is an increasing turbidity from the clear solution state with an increasing number of cycles.<sup>45</sup>

This property was investigated by us<sup>44</sup> with the aim of designing a breast phantom, which led to an optimization of the number of freeze-thaw cycles to obtain reduced scattering coefficients ( $\mu'_s$ ) close to breast tissue literature values. In addition, we measured other optical properties relevant to photoacoustics such as absorption coefficient ( $\mu_a$ ), scattering anisotropy, and refractive index, and found these to be substantially approximate to literature values for tissue. Acoustic properties such as acoustic velocity, acoustic attenuation, and density were measured and also found to be admissible.<sup>44</sup>

The procedure followed for the preparation of the turbid PVA gels for the tissue phantom is discussed in detail elsewhere.<sup>44</sup> The procedure involves submitting aqueous solutions of 20% by weight PVA to freezing and thawing cycles. One freezing-thawing cycle constitutes refrigeration at  $-20^\circ\text{C}$  for 12 h, followed by a defreezing of the frozen solution at room temperature for 12 h.

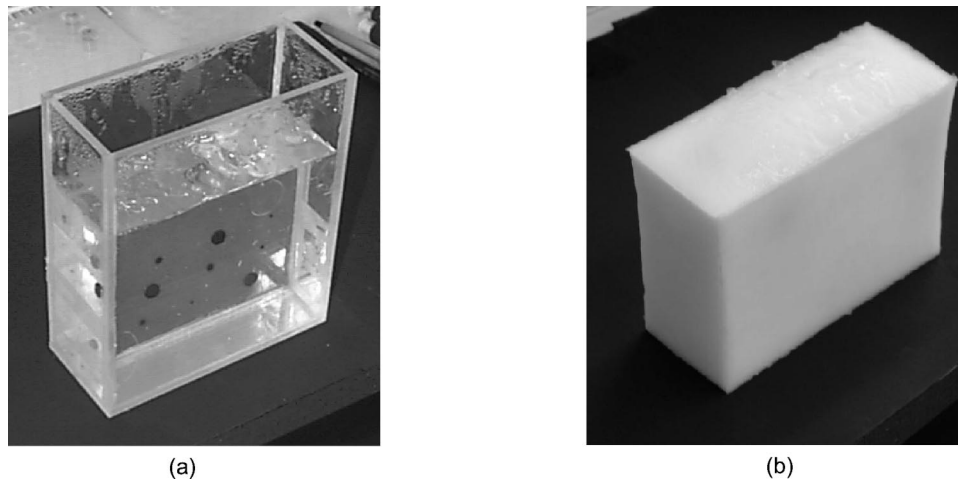


**Fig. 2** (a) The clear aqueous PVA solution in the Perspex mold carries the dyed, rigid PVA gel spheres suspended with nylon thread. The solution is allowed to stand at room temperature for a few hours to allow bubbles to rise to the surface, before it undergoes freezing and thawing cycles. (b) The resulting PVA gel breast phantom after submitting the solution to four freezing-thawing cycles.

### 2.3.2 Dyed gels to simulate tumors—method 2

One of the mechanisms explaining the origin of the turbidity of samples prepared by method 1, has been that of phase separation in the gel. The structure of the gel may be understood to be composed of three distinct phases: a water phase with a low PVA concentration, an amorphous PVA phase, and a crystalline PVA phase.<sup>46</sup> When refrigerated, the water freezes over with an accompanying large volume expansion. This leads to the formation of large pores; the resulting refractive index fluctuations in the medium due predominantly to the presence of these pores leads to the observed turbidity. It was demonstrated by Hyon and Ikada<sup>47</sup> that if the water phase in the gel was prevented from freezing over at the time of refrigeration, it would be possible to obtain a transparent gel. Strong cooling is fundamental to the process of formation of the cross-links and crystallites, and is unavoidable. It was shown that dissolving PVA in a mixture of dimethylsulphoxide (DMSO) and water, and submitting the solution to a single freezing-thawing cycle, yields highly transparent and mechanically strong gels.<sup>48,49</sup> The role of DMSO is to inhibit freezing of the solution.

The procedure followed for the preparation of the dyed samples was similar to the procedure for preparing the transparent gels, which is described in detail in the literature,<sup>44,47,48</sup> with the one exception that a dye was added to the DMSO and water mixture that carries the PVA. Suitable amounts of the dye, Ecoline 700 black watercolor (Royal Talens, Apeldoorn), were added to the solution. An empirical formula was used to determine the amount of dye required for various absorption coefficients ( $\mu_a$ ), from the best fit to the experimentally derived graph of absorption versus concentration of the dye in water. The absorption of the dye in water had been previously ascertained for varying concentrations at 1064 nm, using a spectrophotometer. The resulting dyed solutions were allowed to undergo freezing for 24 h; on thawing, rigid gels were obtained. The resulting samples were then immersed in water to remove the organic solvent. The water was continuously agitated and regularly recharged to promote a thorough exchange of DMSO in the gel with water to yield PVA hydro-

gels. During this process, there was also a release of the dye in the water by diffusion, as was observed by the discoloration of the water. The discharge of the dye reduced after a few days. Three series of gels were prepared with designed  $\mu_a$  of 0.2, 0.1, and 0.05  $\text{mm}^{-1}$ . The samples in each series were fashioned into spheres of sizes 10, 5, and 2 mm in diameter.

### 2.3.3 Finished breast phantom

The strategy to create the breast phantom with the embedded inhomogeneities was to first prepare the dyed spheres by method 2. These were then suspended using 80- $\mu\text{m}$  nylon thread in a Perspex mold of size approximately  $150 \times 60 \times 180$  mm dimensions. The mold with its spheres was kept in a tank under water to keep the gels moist. The procedure for making the tissue component of the phantom, method 1, was then executed. The aqueous PVA solution was removed from the heat and allowed to stand for a while as it cooled. When the average temperature had fallen to 45°C, the solution was carefully poured into the mold along its sides, up to a height of 120 mm. It was necessary for the solution to be cool enough to not soften the inhomogeneities (glass transition temperature  $T_g \approx 60^\circ\text{C}$ ), yet sufficiently high for the solution to be mobile enough to be poured. The solution in the mold shown in Fig. 2(a) was then made to undergo four freezing and thawing cycles to realize the finished breast phantom shown in Fig. 2(b). It is expected that the breast phantom has a reduced scattering coefficient  $\mu'_s \approx 0.5 \text{ mm}^{-1}$  at 1064 nm, which is fairly close to that which is typically quoted for breast tissue (0.6 to 1.1  $\text{mm}^{-1}$ ).<sup>2,50</sup> The relevant optical properties of the phantom compared to breast literature values are consolidated in Table 2.

## 2.4 Experimental Details

### 2.4.1 Spectroscopic studies of dyed gels

The actual  $\mu_a$  of the dyed gels with respect to gels prepared by method 1, were studied using a spectrophotometer (Shimadzu UV-3101 PC, Tokyo), after 2 to 3 weeks of solvent exchange in water. The gels were melted down by heating in

**Table 2** Relevant optical properties of the phantom compared with literature values for breast tissue. The effective attenuation coefficient  $\mu_e = [3\mu_a(\mu_a + \mu_s')]^{1/2}$ . Literature values for breast tissue were taken from Refs. 2 and 50.

	Reduced scattering coefficient ( $\mu_s'$ )	Absorption coefficient ( $\mu_a$ )	Effective attenuation coefficient ( $\mu_e$ )
Phantom (at 1064 nm)	0.5 mm <sup>-1</sup>	0.0342 mm <sup>-1</sup>	0.234 mm <sup>-1</sup>
breast tissue	0.6–1.1 mm <sup>-1</sup>	0.005–0.015 mm <sup>-1</sup>	0.166–0.223 mm <sup>-1</sup>

sealed vessels to around 90°C, poured into 10-mm path-length microcuvettes, and the absorption spectrum was then measured. Melting ensured that the turbid gel was no longer scattering, so that the attenuation through the sample could be attributed only to absorption. Beer-Lambert's law was applied to obtain  $\mu_a$  for the gels from method 1 as shown in Fig. 3(a), and for the three series from method 2 as shown in Fig. 3(b). The absorption contrast at 1064 nm for each series was calculated from the ratio of  $\mu_a$  and that obtained for method 1 samples, and is indicated against each curve in Fig. 3(b). Thus, series 1 comprised samples with a  $\mu_a$  of 0.25 mm<sup>-1</sup>, series 2 with a  $\mu_a$  of 0.136 mm<sup>-1</sup>, and series 3 with  $\mu_a$  of 0.072 mm<sup>-1</sup> at 1064 nm; and absorption contrasts of approximately 7, 4, and 2, respectively, with respect to the background.

#### 2.4.2 Photoacoustic studies

The solid phantom was placed at the bottom of the Perspex tank face down, as shown in Fig. 1(b), so that the distance between the free surface of the phantom and the detector unit on which it rests is 60 mm. The tank was filled with water to keep the phantom moist, and to provide a good acoustic coupling to the detector matrix. The LLG was positioned at a certain point above the phantom. The light energy was 50 mJ per pulse; the separation between the LLG and the phantom was adjusted to allow the beam to expand to approximately 15

mm, providing a laser fluence at the phantom surface of around 20 mJ/cm<sup>2</sup>. For this position of the LLG, a set of 120 elements was accessed beneath the phantom, 12 in the  $x$  direction and 10 in the  $y$  direction. One element was accessed at a time, averaging the signal 128 times. This covered an area of approximately 37×31 mm. The data from this set constituted a volume of interest (VOI). The LLG was then moved to another position and another VOI adjacent to the first was imaged; other such VOIs were recorded in sequence to achieve complete coverage of the phantom.

### 3 Results

#### 3.1 Raw Signals

The graph in Fig. 4 shows a signal trace recorded by a detector element from the volume of interest (VOI) containing the 2-mm sphere at a depth of 15 mm. The trace is obtained by averaging 128 times. The top  $x$  axis has the times of flight of the signal, which can be converted into equivalent distances via the speed of sound in the phantom and marked on the bottom  $x$  axis. The origin of the  $x$  axis corresponds to the position of the detector element. The 18.6-mm-thick protective layer is indicated in the graph by the dotted line at left. Beyond this point the signal trace originates from within the phantom.

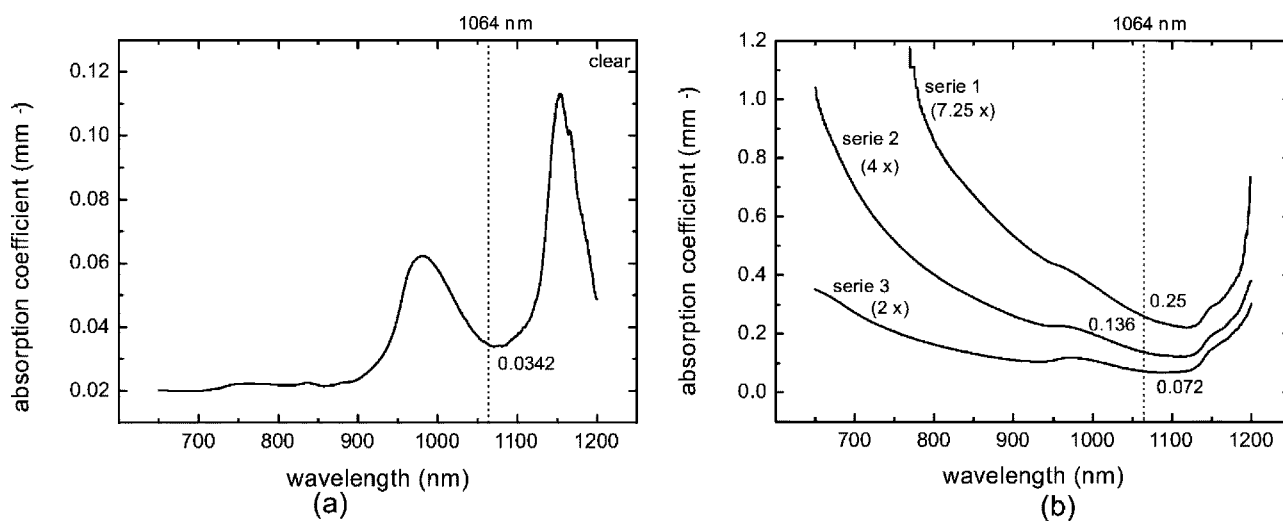


**Fig. 3** Wavelength dependence of absorption coefficients of (a) melted-down and optically clear freeze-thawed PVA gel samples, and (b) melted-down dyed PVA gel samples. The absorption coefficients at 1064 nm are marked in the graphs, and the absorption contrasts of the dyed samples obtained from these values with respect to the clear sample are indicated against each curve.

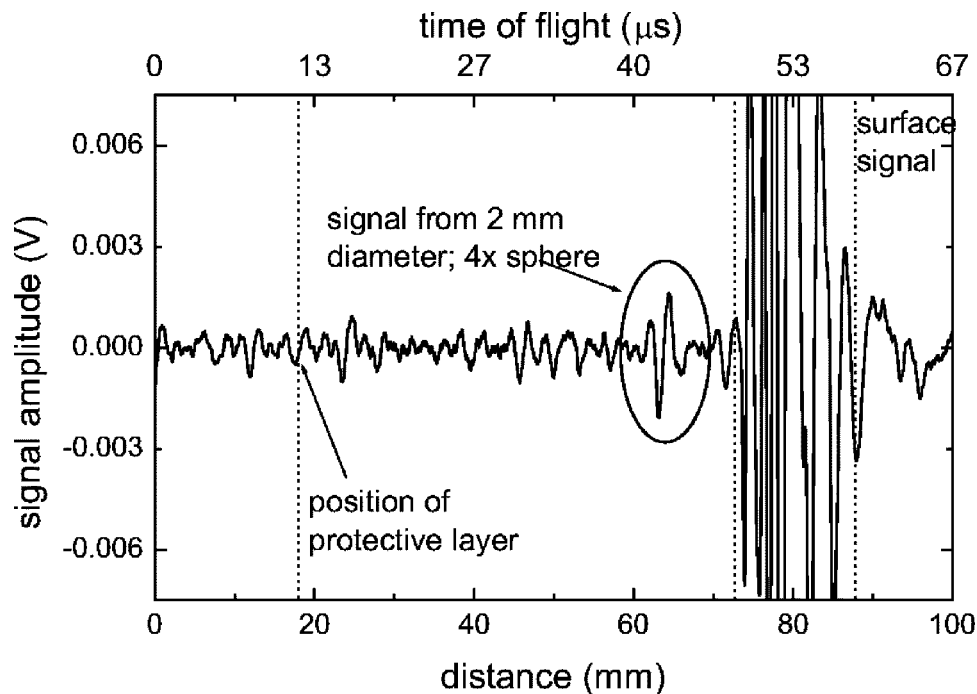


**Fig. 4** Signal traces from an element in the volume of interest (VOI) that contained the 2-mm-diam sphere with absorption contrast 4 at a depth of 15 mm from the illuminated surface of the phantom. The graph has been zoomed in on the Y axis to elucidate the transient arising from the sphere; the surface signal is clipped in the figure.

Two sharp features are evident in the trace: 1. a strong signal at the phantom surface, (shown clipped in the graph), and 2. a bipolar signal at a depth of 15 mm from the phantom surface.

Feature 1 is the photoacoustic signal due to absorption at the free boundary between the phantom and water/air. This is due to the high laser fluence rate at the surface, and the finite absorption coefficient of the phantom. This signal can be used to identify the surface of the phantom.

The second pressure disturbance is from the 2-mm-diam sphere with an absorption contrast ( $4\times$ ) that is known to be present in the VOI at a depth of 15 mm from the illuminated phantom surface. The bipolar nature of the transient is the signature of a spherical absorber as predicted by theory. However, the signal trace in Fig. 4 is noisy with a signal-to-noise ratio (SNR) of the order of 2 to 3, which does not permit the derivation of the size of the sphere accurately, as predicted from Eq. (4).

### 3.2 Image Reconstruction

The raw signals from each VOI in turn are fed to the image reconstruction program, which implements the delay-and-sum beamforming algorithm in Matlab 6.5 (The MathWorks, Incorporated, Natick, Massachusetts). The other inputs to the program are the simulated directivities of a square element ( $2\times 2$ ) mm square for various depths from 0 to 80 mm in discrete steps. For calculations of weight factors for other depths, a process of interpolation is used. The voxel size was chosen for all VOIs as  $1\times 1\times 1$  mm in  $x$ ,  $y$ , and  $z$  directions. The reconstruction is available as 2-D slices of data with  $x$  and  $y$  axes corresponding to the VOI area covered, and each slice separated by 1 mm in the  $z$  direction. In the procedure

for the reconstruction, the entire dataset is normalized to the largest signal intensity in the data matrix. For this reason, the surface signal was excluded (between dotted lines on the right of Fig. 4) in the reconstructions, which would otherwise result in a deterioration in the visualization of weaker sources.

### 3.3 Volume Visualization

The reconstruction of signals from each VOI yields a collection of slices built through the 3-D subvolume. These volume data are visualized by projecting the data values within the matrix onto a viewing plane. Each pixel stores the average value encountered through the voxels in all slices along a viewing ray, and is called an average intensity projection (AIP). This method of visualization is objective and does not require the specification of threshold values.

Figures 5 and 6 are the AIPs of selected VOIs of the phantom. No additional processing was performed on the reconstructed slices. Figure 5 shows the AIP in isometric view for VOIs containing (from left to right): the 2-mm-diam sphere (absorption contrast 4) at a depth of 15 mm from the illuminated surface; the 5-mm-diam sphere with contrast 7 at depth 30 mm; and the 2-mm sphere with contrast 7 at depth 32 mm. Figure 6 shows the corresponding top view AIP for the VOIs of Fig. 5. The left and middle images of Figs. 5 and 6 show lack of background noise because the raw photoacoustic signals that contributed to image formation were received with a good SNR (see Fig. 4).

## 4 Discussion and Conclusion

### 4.1 Breast Tissue Phantom

The novel phantom based on poly(vinyl alcohol) gel has the advantage that it is inherently light scattering with the prepa-

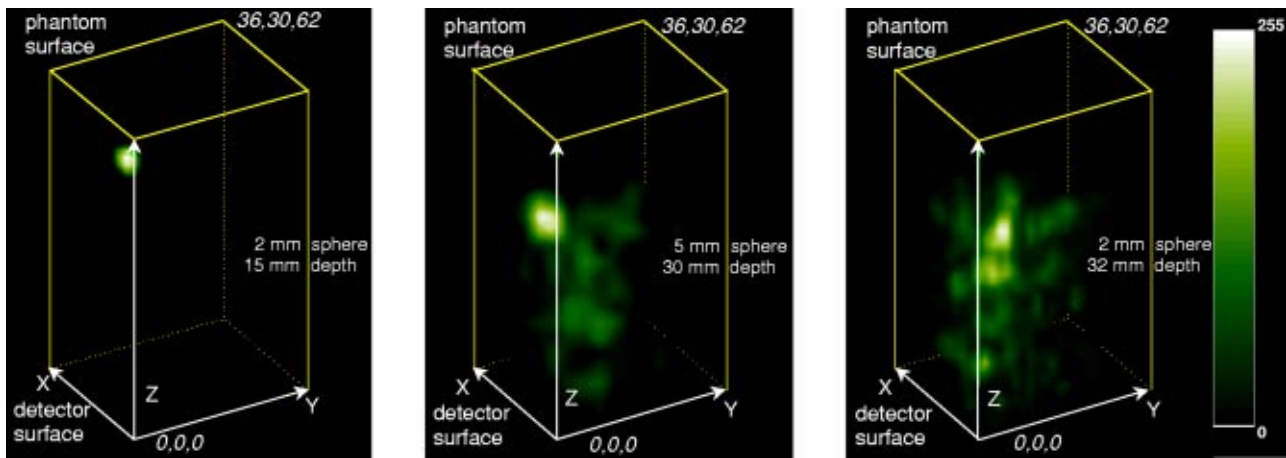


**Fig. 5** Average intensity projections (AIP) in isometric view of the 3-D reconstructed data of selected volumes of interest (VOIs) in the phantom. At left, the VOI containing the 2-mm-diam sphere of absorption contrast 4 at a depth of 15 mm from the illuminated phantom surface. In the center, VOI with 5-mm-diam sphere with contrast 7 and 30 mm from surface. At right, VOI with 2-mm-diam sphere with contrast 7 and depth 32 mm from surface.

ration procedure. This precludes the additional effort and expense incurred with introducing scattering particles in the medium as in conventional gel phantoms. Additionally, the phantom has superior mechanical properties compared with phantoms based on agarose, gelatin, and polyacrylamide. PVA gels are rubbery with a high modulus of elasticity; conventional gels are fragile and may rupture under pressure.

The issue of dye discharge from the gel spheres into the surrounding phantom is important, since this will change the properties of the inclusions with time. The procedure for the preparation of the dyed PVA gel spheres involved addition of the dye (Ecoline 700 black water color) to the mixed solvent of DMSO and water, in which PVA is dissolved. Ecoline 700 is a mixture of water-soluble dyes possessing molecular dimensions of the order of nanometers, which would cause their diffusion out of the gel. As detailed earlier, after its formation, the dyed gel was immersed in water to remove DMSO from the gel. During this period of 2 weeks, the water was agitated continuously and renewed every day. It was assumed that the major part of dye discharge would occur during this period, so that for spheres subsequently embedded in the gel, the dye would stay fairly well confined over time. However, spectrophotometric measurements of spheres resected from the phantom after 1 year showed lower absorption coefficients in the regions below 900 nm; above this the absorption was virtually unchanged. We speculate that the components of the dye that absorb between 600 and 900 nm possess relatively smaller

molecular sizes, which may account for their selective diffusion in the time period studied. Though this may not have affected our present PA measurements at 1064 nm, the use of a substitute absorbing agent such as India ink (composed of carbon black particles with sizes less than 500 nm) will be investigated for future phantom development.

Certain caveats with PVA gel phantoms relate to their use and storage. PVA hydrogels undergo desiccation when exposed to air, causing degradation in their optical properties. For this reason it is imperative that the gels be stored under water. To prevent dehydration during imaging, the phantom was retained in water. Alternatively, a layer of ultrasound gel around the sample may also be used to prevent dehydration. PVA gels are also susceptible to proliferation of fungal growth. This can be avoided by storing the phantoms in a 0.01% solution of sodium azide. (Sodium azide is injurious to human health, and adequate precautions must be taken while handling the solution.) Additionally, sodium azide may also be added to the aqueous PVA solution at the time of formation of the gel. Interestingly, the samples prepared by method 2 were resistant to fungus, possibly due to remnant DMSO, which may possess fungicidal properties.

#### 4.2 Photoacoustic Instrument

The photoacoustic instrument built around the Achilles In-Sight™ detector matrix appears promising. Coupled with the

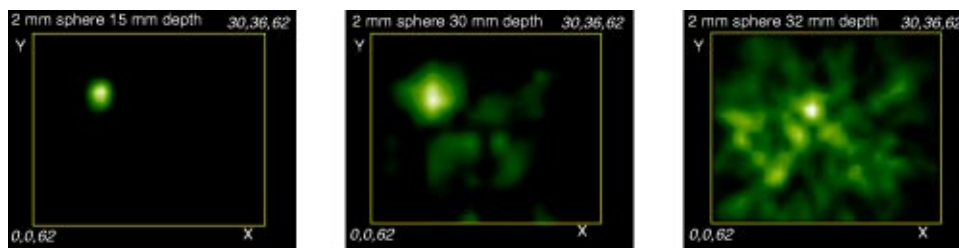


**Fig. 6** Top views of the average intensity projection (AIP) for the same VOIs shown in Fig. 5.

delay-and-sum beamforming algorithm, inhomogeneities as small as 2 mm in diameter and with an absorption contrast of 7 with respect to the background at depths around 32 mm have been detectable in well-characterized breast phantoms. The imaging system is capable of a spatial resolution of 3.5 mm at a distance of 30 mm to the detector, with a scanned area of  $37 \times 31$  mm.<sup>51</sup> The method of projections is an objective manner of visualizing the reconstructed data compared with the isosurface method, which requires the specification of threshold values.

The measurement time is 20 min for a VOI covering  $10 \times 12$  elements, which is approximately  $37 \times 31$  mm. The reason for this is that the signals were averaged up to 128 times for each element, and that only one element of the matrix was accessed at a time. The measurement time will dictate the future design of the patient-instrument interface, to permit the patient to lie prone during breast scanning. In any case, the use of wavelet denoising, for example, is being considered, which should preclude the high number of signal averages used in the present study. Coupled with the availability of up to 10 elements in parallel, which is being implemented at this time, we should achieve considerably shorter measurement times in the future. The sensitivity of the matrix imparts an imaging depth between 35 to 40 mm.<sup>51</sup> The clinical version of the mammoscope will take this into account to provide a facility of interchanging the illumination and detection sides for thicker breasts. Thus a second antipodal view may be necessary to get complete depth coverage of the breast.

Regarding other instrumental changes that are planned, the use of liquid light guides (LLG) will be discontinued. Although they have many attractive advantages, particularly the ease with which an LLG may be coupled to the laser output, they do not possess very high power handling capacity. This leads to the formation of bubbles due to thermal decomposition of the liquid, which affects the transmission of light and quickly worsens with use. The direct laser beam delivered with the use of mirrors is being considered to replace the LLGs.

It is as yet early to draw conclusions about the applicability of the prototype to detect tumors in the breast. Although efforts have been made to choose a phantom with the effective acoustic and optical attributes of the breast, the properties of breast tissue have a wide spread of values depending on age, hormonal status, and medical history of the subject. Additionally, the breast is highly complex and heterogenous both optically and acoustically, factors that have not been taken into account in the design of the phantom used in the present study. These are aspects that we intend to concentrate on in our future research, by imaging inhomogeneous phantoms embedded with inserts of varying geometries and absorption coefficients.

### Acknowledgments

We thank Rich Morris, Steve Morris, and David Ergun of GE Medical Systems Lunar for useful discussions. We thank Theo Pünt and Hans de Boer of the Mechanical and Physical Engineering workshop for their ideas and support in the development of the prototype. Berry Westerhof of Schaeffler Nederland B.V. is acknowledged for illuminating discussions. The research was supported by the European Commission through the projects OPTIMAMM (contract QLG1-CT-2000-00690,

coordinator H. H. Rinneberg) and MEDPHOT (contract QLG1-CT-2000-01464, coordinator R. Steiner).

### References

1. S. J. Nass, I. C. Henderson, and J. C. Lashof, "Mammography and beyond: Developing technologies for the early detection of breast cancer," Report of the Institute of Medicine, National Academy Press, Washington D.C. (2001).
2. B. J. Tromberg, N. Shah, R. Lanning, A. Cerussi, J. Espinoza, T. Pham, L. Svaasand, and J. Butler, "Non-invasive *in vivo* characterization of breast tumours using photon migration spectroscopy," *Neoplasia* **2**(1), 26–40 (2000).
3. B. W. Pogue, S. P. Poplack, T. O. McBride, W. A. Wells, K. S. Osterman, U. L. Osterberg, and K. D. Paulsen, "Quantitative hemoglobin tomography with diffuse near-infrared spectroscopy: Pilot results in the breast," *Radiology* **218**(1), 261–266 (2001).
4. T. McBride, B. W. Pogue, S. Jiang, U. L. Osterberg, K. D. Paulsen, and S. P. Poplack, "Initial studies of *in vivo* absorbing and scattering heterogeneity in near-infrared tomographic breast imaging," *Opt. Lett.* **26**(11), 822–824 (2001).
5. V. Ntziachristos, A. G. Yodh, M. Schnall, and B. Chance, "Concurrent MRI and diffuse optical tomography of breast after Indocyanine Green enhancement," *Proc. Natl. Acad. Sci. U.S.A.* **97**(6), 2767–2772 (2000).
6. X. Intes, J. Ripoll, Y. Chen, S. Nioka, A. G. Yodh, and B. Chance, "In vivo continuous-wave optical breast imaging enhanced with Indocyanine Green," *Med. Phys.* **30**(6), 1039–1047 (2003).
7. J. H. Hoogenraad, M. B. van der Mark, S. B. Colak, G. W. 't Hooft, and E. S. van der Linden, "First results from the Philips optical mammoscope," *Proc. SPIE* **3194**, 184–190 (1998).
8. S. B. Colak, M. B. van der Mark, G. W. 't Hooft, J. H. Hoogenraad, E. S. van der Linden, and F. A. Kuijpers, "Clinical optical tomography and NIR spectroscopy for breast cancer detection," *IEEE J. Sel. Top. Quantum Electron.* **5**(4), 1143–1158 (1999).
9. V. Ntziachristos, X. H. Ma, and B. Chance, "Time-correlated single photon counting imager for simultaneous magnetic resonance and near-infrared mammography," *Rev. Sci. Instrum.* **69**(12), 4221–4233 (1998).
10. D. Grosenick, H. Wabnitz, H. H. Rinneberg, K. T. Moesta, and P. M. Schlag, "Development of a time-domain optical mammograph and first *in vivo* applications," *Appl. Opt.* **38**(12), 2927–2943 (1999).
11. S. Fantini, K. T. Moesta, M. A. Franceschini, H. Jess, H. Erdl, E. Gratton, P. M. Schlag, and M. Kaschke, "Instrumentation and clinical applications in frequency-domain optical mammography," *Proc. 19th Ann. Intl. Conf. IEEE Eng. Med. Biol. Soc.* **6**, 2741–2744 (1997).
12. B. W. Pogue, M. Testorf, T. McBride, U. Osterberg, and K. Paulsen, "Instrumentation and design of a frequency-domain diffuse optical tomography imager for breast cancer detection," *Opt. Express* **1**(13), 391–403 (1997).
13. A. A. Oraevsky, E. V. Savateeva, S. V. Solomatina, A. A. Karabutov, V. G. Andreev, Z. Gatalica, T. Khampirad, and P. M. Henrichs, "Optoacoustic imaging of blood for visualization and diagnostics of breast cancer," *Proc. SPIE* **4618**, 81–94 (2002).
14. A. Oraevsky, V. G. Andreev, A. A. Karabutov, S. V. Solomatina, E. V. Savateeva, R. D. Fleming, Z. Gatalica, and H. Singh, "Laser optoacoustic imaging of breast cancer *in vivo*," *Proc. SPIE* **4256**, 6–15 (2001).
15. R. A. Kruger, W. L. Kiser, Jr., D. R. Reinecke, and G. A. Kruger, "Application of thermoacoustic computed tomography to breast imaging," *Proc. SPIE* **3659**, 426–430 (1999).
16. R. A. Kruger, K. D. Miller, H. E. Reynolds, W. L. Kiser Jr., D. R. Reinecke, and G. A. Kruger, "Breast cancer *in vivo* contrast enhancement with thermoacoustic CT at 434 MHz.—a feasibility study," *Radiology* **216**(1), 279–283 (2000).
17. R. A. Kruger, W. L. Kiser, Jr., A. P. Romilly, and P. Schmidt, "Thermoacoustic CT of the breast: Pilot study observations," *Proc. SPIE* **4256**, 1–5 (2001).
18. A. A. Oraevsky, S. L. Jacques, and R. O. Esenaliev, "Optoacoustic imaging for medical diagnosis," U.S. Patent No. 5,840,023 (1998).
19. R. A. Kruger, "Photoacoustic breast scanner," U.S. Patent No. 5,713,356 (1998).
20. T. Bowen, "Radiation induced thermoacoustic soft tissue imaging," *Proc.-IEEE Ultrason. Symp.* **2**, 817–822 (1981).
21. T. Bowen, R. L. Nasoni, A. E. Pifer, and G. H. Sembrski, "Some

- experimental results on the thermoacoustic imaging of tissue equivalent phantom materials," *Proc.-IEEE Ultrason. Symp.* **2**, 823–827 (1981).
22. R. A. Kruger, "Photo-acoustic ultrasound: Pulse production and detection in 0.5% Liposyn," *Med. Phys.* **21**(7), 1179–1184 (1994).
  23. A. A. Oraevsky, S. L. Jacques, R. O. Esenaliev, and F. K. Tittel, "Time resolved optoacoustic imaging in layered biological tissues," *Proc. Opt. Soc. Amer. (OSA)* **21**, 161–165 (1994).
  24. X. Wang, Y. Pang, G. Ku, X. Xie, G. Stoica, and L. H. Wang, "Non-invasive laser-induced photoacoustic tomography for structural and functional imaging of the brain *in vivo*," *Nat. Biotechnol.* **21**(7), 803–806 (2003).
  25. R. A. Kruger, W. L. Kiser, Jr., D. R. Reinecke, G. A. Kruger, and K. D. Miller, "Thermoacoustic optical molecular imaging of small animals," *Molecular Imag.* **2**(2), 113–123 (2003).
  26. R. G. M. Kolkman, E. Hondebrink, W. Steenbergen, and F. F. M. de Mul, "In vivo photoacoustic imaging of blood vessels using an extreme-narrow aperture sensor," *IEEE J. Sel. Top. Quantum Electron.* **9**(2), 343–346 (2003).
  27. G. Schüle, G. Hüttmann, C. Framme, J. Roeder, and R. Brinkmann, "Noninvasive optoacoustic temperature determination at the fundus of the eye during laser irradiation," *J. Biomed. Opt.* **9**(1), 173–179 (2004).
  28. U. Oberheide, I. Bruder, H. Welling, W. Ertmer, and H. Lubatschowski, "Optoacoustic imaging for optimization of laser cyclophotocoagulation," *J. Biomed. Opt.* **8**(2), 281–287 (2003).
  29. M. Yamazaki, S. Sato, D. Saito, Y. Okada, A. Kurita, M. Kikuchi, H. Ashida, and M. Obara, "Photoacoustic diagnosis of burns in rats: Two-dimensional photo-acoustic imaging of burned tissue," *Proc. SPIE* **4960**, 7–13 (2003).
  30. J. A. Viator, C. Bernard, M. Ambrose, J. Spanier, and J. N. Nelson, "In vivo port-wine stain depth determination with a photoacoustic probe," *Appl. Opt.* **42**(16), 3215–3224 (2003).
  31. Z. Zhao and R. Myllylä, "Photoacoustic blood glucose and skin measurement based on optical scattering effect," *Proc. SPIE* **4707**, 153–157 (2002).
  32. A. A. Bednov, E. V. Savateeva, and A. A. Oraevsky, "Glucose monitoring in whole blood by measuring laser-induced acoustic profiles," *Proc. SPIE* **4960**, 21–29 (2003).
  33. R. O. Esenaliev, I. Larina, K. V. Larin, D. J. Deyo, M. Motamedi, and D. S. Prough, "Optoacoustic technique for noninvasive monitoring of blood oxygenation: A feasibility study," *Appl. Opt.* **41**(22), 4722–4731 (2002).
  34. E. V. Savateeva, A. A. Karabutov, S. V. Solomatina, and A. A. Oraevsky, "Optical properties of blood at various levels of oxygenation studied by time-resolved detection of laser-induced pressure profiles," *Proc. SPIE* **4618**, 63–75 (2002).
  35. M. W. Sigrist and F. K. Kneubühl, "Laser-generated stress waves in liquids," *J. Acoust. Soc. Am.* **64**(6), 1652–1663 (1978).
  36. C. G. A. Hoelen and F. F. M. de Mul, "A new theoretical approach to photoacoustic signal generation," *J. Acoust. Soc. Am.* **106**(2), 695–706 (1999).
  37. C. G. A. Hoelen, A. Dekker, and F. F. M. de Mul, "Detection of photoacoustic transients originating from microstructures in optically diffuse media such as biological tissue," *IEEE Trans. Ultrason. Ferroelectr. Freq. Control* **48**(1), 37–47 (2001).
  38. V. G. Andreev, A. A. Karabutov, and A. A. Oraevsky, "Detection of ultrawide-band ultrasound pulses in optoacoustic tomography," *IEEE Trans. Ultrason. Ferroelectr. Freq. Control* **50**(10), 1383–1390 (2003).
  39. P. C. Beard, F. Perennes, E. Draguioi, and T. N. Mills, "Optical fiber photoacoustic-photothermal probe," *Opt. Lett.* **23**(15), 1235–1237 (1998).
  40. G. Paltauf and H. Schmidt-Kloiber, "Measurement of laser-induced acoustic waves with a calibrated optical transducer," *J. Appl. Phys.* **82**(4), 1525–1531 (1997).
  41. G. Paltauf, H. Schmidt-Kloiber, K. P. Kostli, and M. Frenz, "Optical method for two-dimensional ultrasonic detection," *Appl. Phys. Lett.* **75**(8), 1048–1050 (1999).
  42. B. P. Payne, V. Venugopalan, B. B. Mikic, and N. S. Nishioka, "Optoacoustic tomography using time-resolved interferometric detection of surface displacement," *J. Biomed. Opt.* **8**(2), 273–280 (2003).
  43. C. G. A. Hoelen and F. F. M. de Mul, "Image reconstruction for photoacoustic scanning of tissue structures," *Appl. Opt.* **39**(31), 5872–5883 (2000).
  44. A. Kharine, S. Manohar, R. Seeton, R. G. M. Kolkman, R. A. Bolt, W. Steenbergen, and F. F. M. de Mul, "Poly(vinyl alcohol) gels for use as tissue phantoms in photoacoustic mammography," *Phys. Med. Biol.* **48**(3), 357–370 (2003).
  45. N. A. Peppas, "Turbidimetric studies of aqueous poly(vinyl alcohol) solutions," *Makromol. Chem.* **176**(11), 3433–3440 (1975).
  46. C. M. Hassan and N. A. Peppas, "Structure and applications of poly(vinyl alcohol) hydrogels produced by conventional crosslinking or by freezing/thawing methods," *Adv. Polym. Sci.* **153**, 37–65 (2000).
  47. S. H. Hyon and Y. Ikada, "Porous and transparent poly(vinyl alcohol) gel and method of manufacturing the same," U.S. Patent No. 4,663,358 (1987).
  48. S. H. Hyon, W. I. Cha, and Y. Ikada, "Preparation of transparent poly(vinyl alcohol) hydrogel," *Polym. Bull.* **22**(2), 119–122 (1989).
  49. S. H. Hyon, W. I. Cha, Y. Ikada, M. Kita, Y. Ogura, and Y. Honda, "Poly(vinyl alcohol) as soft contact lens material," *J. Biomater. Sci. Polymer Edn.* **5**(5), 397–406 (1994).
  50. K. Suzuki, Y. Yamashita, K. Ohta, M. Kaneko, M. Yoshida, and B. Chance, "Quantitative measurement of optical parameters in normal breasts using time-resolved spectroscopy: In vivo results of 30 Japanese women," *J. Biomed. Opt.* **1**(3), 330–334 (1996).
  51. A. Kharine, S. Manohar, W. S. Steenbergen, and T. G. van Leeuwen (*manuscript in preparation*).